Design of a back-illuminated, crystallographically etched, silicon-on-sapphire avalanche photodiode with monolithically integrated microlens, for dual-mode passive & active imaging arrays

A.G. Stern*[a], Daniel C. Cole[b]
[a]Dept. of Electrical Eng., Boston Univ., 8 St. Mary's St., Boston, MA, USA 02215;
[b]Dept. of Manufacturing Eng., Boston Univ., 15 St. Mary's St., Brookline, MA, USA 02446;

ABSTRACT

There is a growing need in space and environmental research applications for dual-mode, passive and active 2D and 3D ladar imaging methods. To fill this need, an advanced back-illuminated avalanche photodiode (APD) design is presented based on crystallographically etched (100) epitaxial silicon on R-plane sapphire (SOS), enabling single photon sensitive, solid-state focal plane arrays (FPAs) with wide dynamic range, supporting passive and active imaging capability in a single FPA. When (100) silicon is properly etched with KOH:IPA:H_2O solution through a thermally grown oxide mask, square based pyramidal frustum or mesa arrays result with the four mesa sidewalls of the APD formed by (111) silicon planes that intersect the (100) planes at a crystallographic angle, $\phi_c = 54.7°$. The APD device is fabricated in the mesa using conventional silicon processing technology. Detectors are back-illuminated through light focusing microlenses fabricated in the thinned, AR-coated sapphire substrate. The APDs share a common, front-side anode contact, made locally at the base of each device mesa. A low resistance (Al) or (Cu) metal anode grid fills the space between pixels and also inhibits optical cross-talk. SOS-APD arrays are indium bump-bonded to CMOS readout ICs to produce hybrid FPAs. The quantum efficiency for the square 27 μm pixels exceeds 50% for 250 nm < λ < 400 nm and exceeds 80% for 400 nm < λ < 700 nm. The sapphire microlenses compensate detector quantum efficiency loss resulting from the mesa geometry and yield 100% sensitive-area-fill-factor arrays, limited in size only by the wafer diameter.

Keywords: silicon APD arrays, back-illuminated, high quantum efficiency, silicon-on-sapphire, crystallographically selective etching, monolithic sapphire microlens arrays, 100% sensitive-area-fill-factor, zero optical cross-talk

1. INTRODUCTION

We present in this paper a novel back-illuminated APD device design that enables the fabrication of low cost, high-performance silicon APD arrays by supporting high quantum efficiency, square pixels with 27 μm side length for high resolution imaging with 100% sensitive-area-fill-factor, on a mechanically rugged and optically transparent sapphire substrate. When (100) silicon is properly etched with KOH:IPA:H_2O solution through a thermally grown oxide mask, square based pyramidal frustum or mesa arrays result with the four mesa sidewalls of the APD formed by (111) silicon planes that intersect the (100) planes at a crystallographic angle, $\phi_c = 54.7°$. [1] The APD is fabricated in the mesa using conventional silicon processing technology and is specially designed to operate over a wide dynamic range in a dual-mode, operating in a linear mode with or without internal gain for passive imaging in daylight conditions and in single-photon sensitive Geiger-mode for active or passive imaging under low-light level conditions. The detector is back-illuminated through a light focusing spherical microlens fabricated in the thinned sapphire substrate that directs light toward the device interior and away from the silicon mesa sidewalls, thereby compensating the optical dead space between pixels resulting from the mesa isolation etch and also from the internal device guard diode geometry. The sapphire microlenses can be coated with an antireflective λ/4-MgF_2 layer for example, to improve the optical power transmittance from air into the sapphire. In addition, a lattice matched (AlN) antireflective crystal layer can be grown at the sapphire-silicon interface to further increase the optical power transmittance into the device silicon as shown in Fig. 1. The APDs in the array share a common, front-side anode contact, made locally at the base of each device mesa. A low resistance aluminum (Al) or copper (Cu) metal anode grid fills the space between pixels and also functions

*ag_stern@hotmail.com; phone 1 617 669-6029; fax 1 617 353-8381; bu.edu

Lidar Remote Sensing for Environmental Monitoring IX,
Edited by Upendra N. Singh, Kazuhiro Asai, Achuthan Jayaraman, Proc. of SPIE Vol. 7153, 71530Z

CCC code: 0277-786X/08/$18 http://dx.doi.org/10.1117/12.804846

to inhibit optical cross-talk by shielding adjacent detectors from stray photons generated during the avalanche process. SOS-APD arrays are indium bump-bonded to CMOS readout ICs to produce hybrid FPAs as shown in Fig. 2, which might be 1024x1024 pixels or larger. [2,3] The camera lens focal length and focal ratio maintain 100% sensitive-area-fill-factor over the full FPA active area by limiting the maximum incidence angle of the extreme rays shown in red in Fig. 2, incident at the microlens edges of the pixel, located farthest from the camera optic axis at the corner of the FPA.

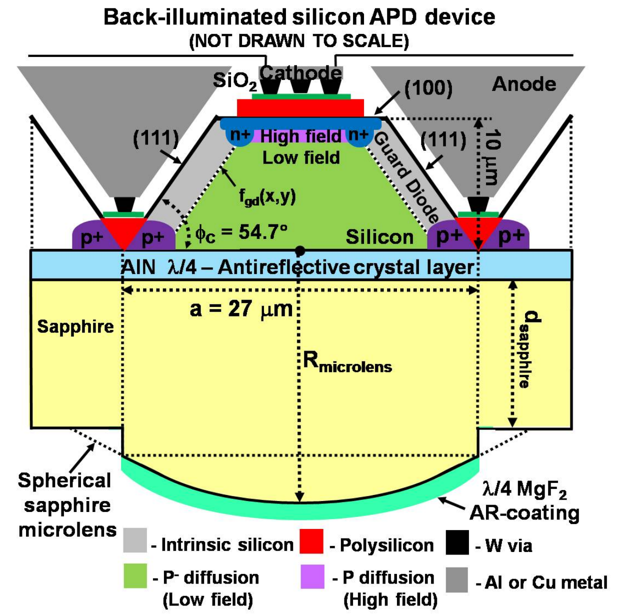

Fig. 1: Advanced back-illuminated, crystallographically etched silicon-on-(R-plane) sapphire APD device for arrays, showing a monolithically integrated sapphire microlens and $\lambda/4$-MgF_2 and AlN antireflective layers.

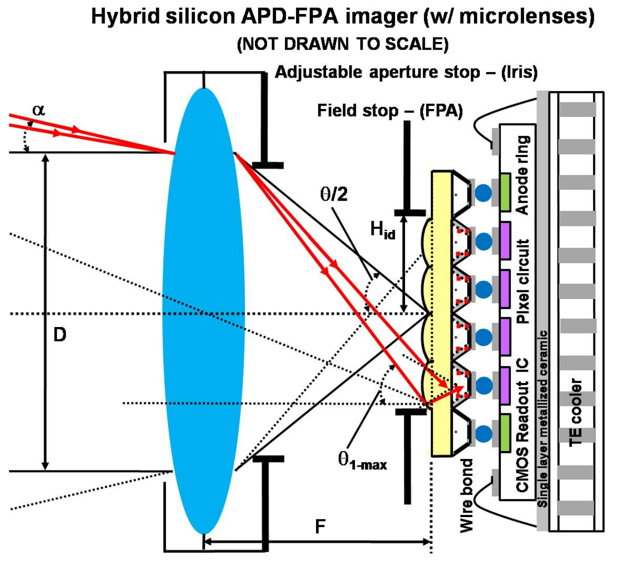

Fig. 2: Back-illuminated, silicon-on-sapphire APD array chip, bump-bonded to CMOS readout-IC. Extreme rays (shown in red) are incident at the maximum incidence angle $\theta_{1\text{-}max}$.

The silicon APD is designed with a carefully optimized high electric field multiplication region, fabricated by high temperature diffusion of boron. The boron impurity profile determines the spatial electric field in the device, and the boundary between the low-electric-field absorption-collection region and the high-electric-field multiplication region, as well as the APD guard diode geometry which is described by the guard diode boundary function $f_{gd}(x,y)$, shown in Fig. 1. The narrow, high electric field multiplication region and the much wider low electric field collection-absorption region, help to provide stable, uniform gain with minimum variance, for nearly all of the photogenerated electrons in the device, and since most electron-hole pairs (EHPs) are generated through light absorption outside of the multiplication region, this results in a low excess noise factor for the APD. [4]

2. SILICON-ON-SAPPHIRE MATERIAL SYSTEM FOR APD ARRAYS

The capability of Czochralski grown R-plane sapphire crystal substrates to support the epitaxial growth of (100) oriented silicon, was discovered in 1963 by researchers at the Boeing corporation. Since the initial discovery, SOS technology has been applied primarily for producing high speed, radiation resistant CMOS circuits for use in space applications. In fact, the microprocessor aboard the Voyager space craft launched in 1977 was fabricated using silicon-on-sapphire and it still continued to function in 2006, three years after the craft had exited the earth's solar system. In the early years of SOS technology, material challenges provided the main obstacle to its rapid commercialization for VLSI-CMOS transistor fabrication. The relatively large lattice mismatch between atoms in the silicon crystal and atoms of the sapphire R-plane, resulted in high defect concentrations in the thin device silicon near the sapphire interface where FET transistors were fabricated. High defect concentrations in the epitaxial silicon led to low process yields early on, that prevented the technology from becoming cost competitive with bulk silicon CMOS processes and as a result, the technology was only used for special applications that could justify the increased cost.

Lidar Remote Sensing for Environmental Monitoring IX,
Edited by Upendra N. Singh, Kazuhiro Asai, Achuthan Jayaraman, Proc. of SPIE Vol. 7153, 71530Z
http://dx.doi.org/10.1117/12.804846

A breakthrough occurred in 1979 with the development of a method to improve the silicon crystal quality at the sapphire interface by ion implanting Si ions using channeling, to amorphise the higher defect density silicon near to the sapphire interface while leaving the higher quality silicon closer to the epitaxial surface undamaged. [5] The substrate was subsequently annealed to recrystallize the silicon near the sapphire interface using the high quality silicon at the top, as a template for crystal growth. By the early 1990s, SOS-CMOS technology had become viable commercially for high speed RF-CMOS circuit applications.

Although silicon-on-sapphire was originally developed for integrated circuit applications, it also has many ideal attributes for use as a substrate material, supporting back-illuminated, solid-state, silicon detector arrays. Sapphire is an anisotropic, dielectric crystal of the negative uniaxial type that is weakly birefringent (n_o-n_e= 0.008) and possesses broadband optical transmittance ranging from the deep ultraviolet (λ_o = 200 nm) to the midwave IR (λ_o = 5500 nm). Sapphire is extremely resilient, supporting thinning below 100 µm which is an important requirement for high resolution back-illuminated detector arrays. Sapphire can be optically polished to better than an 80-50 surface finish and can be etched optically using 157 nm excimer laser ultraviolet light in order to fabricate light focusing microlenses for the silicon detectors. Sapphire is chemically resistant to most liquid etchants at room temperature and therefore functions as an ideal etchstop material during liquid crystallographic etching with KOH:IPA:H_2O solution to define the silicon pixel mesa arrays. To enable high quantum efficiency back-illuminated silicon detector arrays, the refractive index mismatch between air, sapphire and silicon has to be corrected however. The wide bandgap semiconductor material aluminum nitride (AlN), is closely lattice matched and refractive index matched to both sapphire and silicon and offers the prospect of enabling fabrication of high transmittance (100) silicon-on-(AlN)-sapphire substrates for back-illuminated silicon imagers.

2.1 Crystalline lattice matching between silicon, aluminum nitride and sapphire

Sapphire, also known by the alternate designation of α-Al_2O_3, crystallizes in a rhombohedral structure with rhombohedral lattice constant a_R = 5.128 Å and α = 55.28°. The sapphire structure however, is usually described by hexagonal indexing where the expressions in Eq. (1) relate the rhombohedral and hexagonal lattice constants.

$$a_R = \frac{1}{3}\sqrt{3a_H^2 + c_H^2} \qquad \sin\frac{\alpha}{2} = \frac{3}{2\sqrt{3 + \left(c_H / a_H\right)^2}} \tag{1}$$

The hexagonal lattice constants of sapphire are a_H = 4.758 Å and c_H = 12.991 Å. For sapphire, the ratio of c_H/a_H = 2.73. If the ratio were equal to 2.45, then α = 60° and the material would be face center cubic (FCC). Aluminum and oxygen atoms in sapphire are stacked in a bilayer arrangement that repeats after six units of stacking in the c-direction of the bilayers as shown in Fig. 3. [6] Note also that one third of the aluminum atom sites in sapphire are vacant.

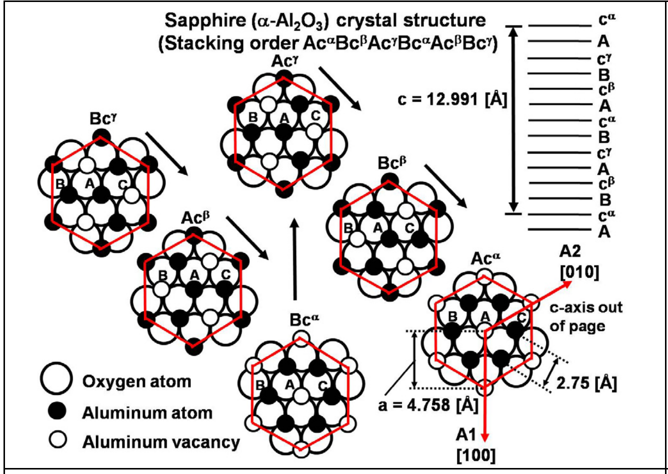

Fig. 3: Stacking of Al and O atomic bilayers in sapphire.

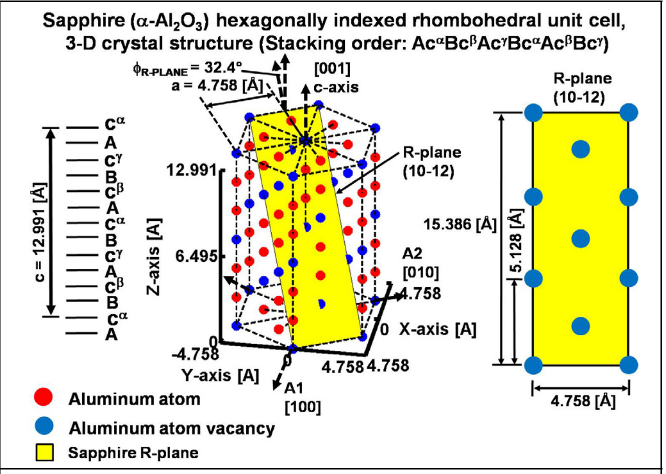

Fig. 4: Al positions on the sapphire R-plane are shown in blue.

Figure 4 shows a three dimensional view of the sapphire unit cell and its hexagonal symmetry. The optic c-axis of sapphire forms an angle of 32.4° with the R-plane which is highlighted in yellow. The Al atom positions shown in blue on the R-plane in Fig. 4 are arranged with almost square FCC symmetry, matching the (100) crystal face of silicon which has a lattice constant $a = 5.431$ Å shown in Fig. 5. The lattice mismatch therefore between (100) silicon and R-plane sapphire is 12.4% in the [010] direction normal to the (-12-10) A-plane and it is 5.6% in the direction parallel to the R-plane and orthogonal to the [010] direction. The magnitude in the percent lattice mismatch between (100) silicon and R-plane sapphire results in a considerable defect density concentration near the interface, thereby precluding direct application of this silicon for devices without first implementing silicon regrowth methods of the type already described, to reduce the defect density.

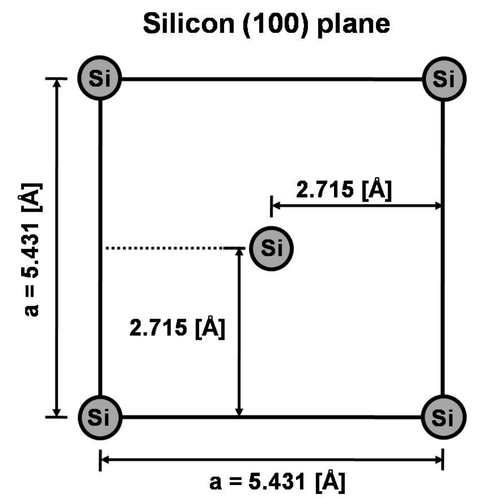

Fig. 5: Silicon atom positions on the (100) silicon plane.

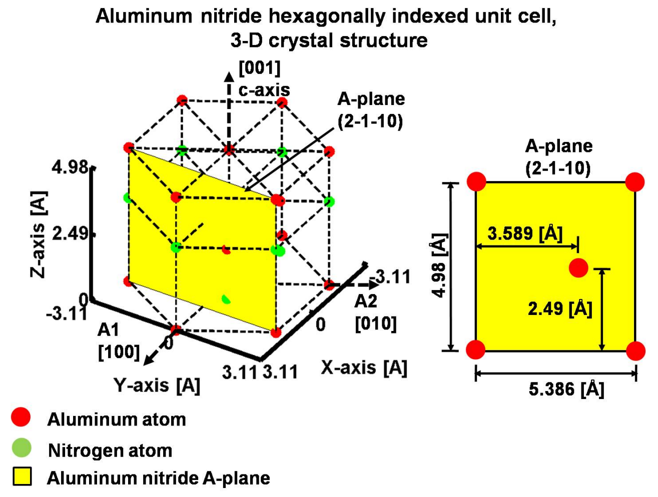

Fig. 6: Al and N positions on the AlN A-plane are indicated.

Aluminum nitride, which is proposed here as a lattice matched single crystal antireflective layer at the silicon-sapphire interface, crystallizes in a Wurzite structure that also possesses hexagonal symmetry with lattice constant $a = 3.11$ Å and $c = 4.98$ Å. Figure 6 shows a three dimensional view of the AlN unit cell and its hexagonal symmetry. The atoms occupying positions in the AlN A-plane highlighted in yellow, match the symmetry of both the sapphire R-plane atoms and the silicon (100) atoms. The lattice mismatch between AlN atoms and R-plane sapphire atoms is 4.8% in the direction parallel to the AlN A-plane and normal to the [100] direction while the mismatch is 4.5% in the [001] c-axis direction of AlN. Also of note is the off-center position of the Al atom in Fig. 6 on the right. Lattice mismatch between AlN atoms and (100) silicon atoms is 0.8% and 8.3% respectively. A review of the literature shows that A-plane AlN can in fact be grown on R-plane sapphire which strengthens the possibility of also being able to grow (100) epitaxial silicon on R-plane sapphire having a thin (< 100 nm thick) lattice matched AlN single crystal antireflective layer. [7] Such epitaxial growth would produce novel silicon-on-(AlN)-sapphire substrates for low-cost, high quantum efficiency, back-illuminated silicon optoelectronics.

2.2 Refractive index matching between silicon, aluminum nitride and sapphire

To minimize reflection losses as light propagates from air into the device silicon through the back-illuminated sapphire substrate, antireflective material layers can be deposited or grown at the air-sapphire and the sapphire-silicon interfaces respectively. At the air-sapphire interface, a single $(\lambda/4)$ MgF_2 antireflective layer provides almost unity optical power transmittance from air into sapphire at the design wavelength. MgF_2 has a low refractive index and is used commonly as an antireflective coating for sapphire and conventional glass optics. At the sapphire silicon interface, AlN provides the required lattice matching between R-plane sapphire and (100) silicon as demonstrated in Sec. 2.1 and in addition, can provide refractive index matching to enhance the optical power transmitted into the device silicon from sapphire over a broad wavelength range.

Aluminum nitride is a birefringent, direct bandgap semiconductor of the positive uniaxial type ($n_o < n_e$), and possesses a room temperature bandgap $E_{g\text{-}AlN} = 6.13$ eV, corresponding to a wavelength $\lambda_{Eg} = (hc_o)/qE_{g\text{-}AlN} = 201.5$ nm. High

Lidar Remote Sensing for Environmental Monitoring IX,
Edited by Upendra N. Singh, Kazuhiro Asai, Achuthan Jayaraman, Proc. of SPIE Vol. 7153, 71530Z

quality crystalline material shows excellent optical transmittance for TE and TM polarized waves and can be considered a lossless dielectric for $\lambda_o \geq 250$ nm. Crystalline AlN is closely lattice matched to sapphire. Unlike sapphire, bulk AlN has proven difficult to prepare and wafers are not commercially available. AlN however, can be readily grown on sapphire substrates by a variety of epitaxial methods including MBE, MOVPE and MOCVD, that allow precise control of the thickness almost to the atomic level, for use as a lattice matching buffer layer to improve the crystalline quality of other materials such as the ternary alloys $Al_xGa_{(1-x)}N$ and $In_xGa_{(1-x)}N$ used in ultra violet-blue-green light emitters. [8] Since AlN has a refractive index intermediate between sapphire and silicon, it could therefore be used as a $\lambda/4$ single crystal anti-reflective layer to improve the back-illuminated optical power transmittance into silicon from sapphire. Crystalline aluminum nitride has a refractive index described by Eq. (2), with constants given for the equation in Table 2.2-1.

$$n_{o,e}^2(\lambda) = 1 + \frac{A_1\lambda^2}{\lambda^2 - \lambda_1^2} \quad \rightarrow (\,\lambda \text{ in nm}\,) \tag{2}$$

Table 2.2-1, from Ref. [9]

		n_o	n_e
$A_1\left(E_{g-AlN}\right) = B_0 + B_1E_{g-AlN} + B_2E_{g-AlN}^2$ $\lambda_1\left(E_{g-AlN}\right) = C_0 + C_1E_{g-AlN} + C_2E_{g-AlN}^2$	B_0	6.626	7.042
	B_1	-0.934	-1.054
	B_2	0.0598	0.0733
	C_0	396.8	381.2
	C_1	-84.12	-76.68
	C_2	6.758	6.068

Equation (2) is a special form of a first order Sellmeier equation with constants parameterized by the optical bandgap of the material. This form of the equation is necessary because it describes the wavelength dependent refractive index as a function of the measured optical bandgap of the AlN crystalline material sample. This description is needed because different preparation methods of AlN will yield different measured refractive indices for the material and the one common denominator that has been successful in reconciling the differences in the experimental data published by different researchers, has been the optical bandgap of the particular AlN sample being studied. [9]

The refractive indices for the dielectrics MgF_2 and sapphire and also AlN, are plotted up to a wavelength of 3 µm in Fig. 7 from published Sellmeier equations, along with the real part of the silicon refractive index.

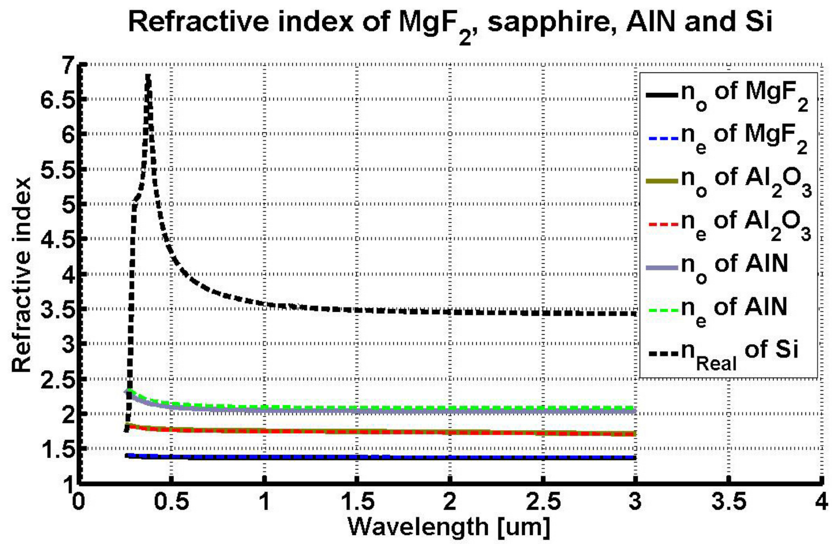

Fig. 7: Real refractive indices for MgF_2, sapphire, AlN and silicon are shown as a function of the optical wavelength.

In contrast to MgF_2, AlN and sapphire, silicon absorbs light in the 200 nm to 1100 nm wavelength range with a long wavelength cutoff set by the indirect bandgap of $E_{g\text{-}Si} = 1.12$ eV at room temperature. Silicon can also be used in solid-state photodetectors to detect soft x-rays with λ_o in the tens of nanometers. The useful range of detected wavelengths for back-illuminated devices fabricated in silicon-on-(AlN)-sapphire substrates however, is limited from 250 nm to 1100 nm by the AlN and silicon bandgaps respectively. The long wavelength cut-off of AlN extends to $\lambda_o = 3$ μm while sapphire and MgF_2 extend beyond $\lambda_o = 5$ μm thereby supporting infrared detection at the optical communications wavelengths of $\lambda_o = 1310$ nm, 1550 nm and beyond, using silicon-germanium or extrinsically doped silicon.

A lossy medium such as silicon, where the lossiness is useful in the context of photodetection applications, cannot be described only by the real refractive index when considering reflection, refraction and propagation of electromagnetic waves in the medium and has to be described by the complex impedance η, that considers the real part of the refractive index and the wavelength dependent absorption coefficient $\alpha(\lambda)$ which quantifies the lossiness of the material. Equation (3) expresses the impedance of a material as a function of the real refractive index $n(\lambda)$, and the absorption coefficient $\alpha(\lambda)$. The expression $0.5(\alpha/k_o)$ in Eq. (3) is known as the extinction coefficient of the material.

$$\eta(\lambda) = \sqrt{\frac{\mu_o}{\varepsilon_o\left(n(\lambda) - j\frac{1}{2}\frac{\alpha(\lambda)}{k_o}\right)^2}} \tag{3}$$

To calculate the optical power transmittance of TE and TM waves into silicon for the back-illuminated MgF_2-sapphire-AlN-silicon substrate, the full wave transfer matrix M_{stack} for the material layers in the substrate has to be obtained. This result needs to be put into a scattering matrix form, that yields the reflection coefficients for the incident waves which in turn allow the reflected and transmitted optical power to be calculated. The wave transfer-scattering matrix theory is described in the text by Saleh & Teich. [10] The matrix M_{stack} for air-(MgF_2)-sapphire-(AlN)-silicon is complicated to calculate and is given by multiplying together seven wave transfer matrices including three for propagation through MgF_2, sapphire, AlN and four matrices for the material interfaces as shown in Eq. (4).

$$M_{\eta-stack} = \begin{bmatrix} A & B \\ C & D \end{bmatrix} = M_7 M_6 M_5 M_4 M_3 M_2 M_1 \tag{4}$$

The matrices M_1, M_3, M_5 and M_7 represent wave transfer matrices at the air-MgF_2, MgF_2-sapphire, sapphire-AlN and AlN-silicon interfaces while matrices M_2, M_4 and M_6 are propagation matrices through MgF_2, sapphire and AlN. All seven matrices are expressed in terms of the complex impedances of the materials given by Eq. (3). Figure 8 shows a polynomial fit to the calculated data for the optical power transmittance of a TE wave from air into silicon.

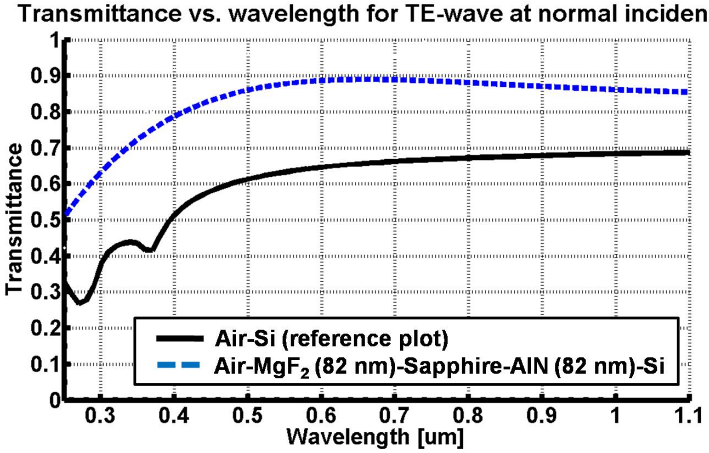

Fig. 8: Optical power transmittance into silicon of a TE wave normally incident from air to the back-illuminated APD substrate.

http://dx.doi.org/10.1117/12.804846

3. HIGH QUANTUM EFFICIECNY SILICON APD ARRAY DESIGN

Silicon on R-plane sapphire substrates support a reliable and low cost method for fabricating large area, high resolution silicon APD arrays with 27 µm pixels or smaller by using the anisotropic, crystallographically selective liquid etchant KOH:IPA:H_2O, to define an array of square based silicon pixels or device mesas that are electrically isolated from each other. The dielectric sapphire substrate acts as a natural etchstop barrier, ensuring that all mesas are uniformly etched to the same height and are fully isolated electrically from each other. Anisotropic, crystallographically selective liquid etching is performed through a hard silicon dioxide mask which is deposited or thermally grown on the epitaxial silicon prior to the crystallographic etching step. Openings are patterned and etched in the hard SiO_2 mask using photolithography and isotropic etching of the SiO_2 with aqueous HF or a buffered oxide etching solution. Figure 9 shows a hard oxide mask with aperture that could be used to crystallographically etch a 3x3 pixel array of APD device mesas. Crystallographic directions for the underlying silicon are also indicated.

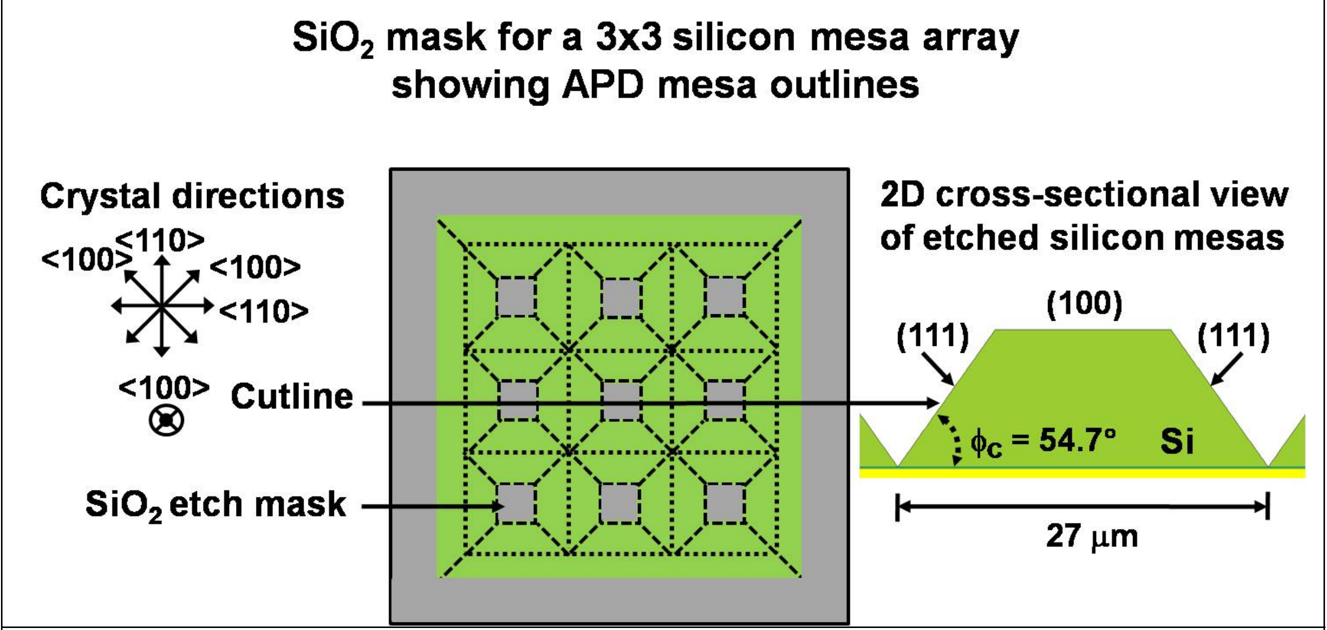

Fig 9: SiO_2 hard mask design showing the aperture for crystallographically etching a square based silicon mesa frustum array.

The silicon crystallographic etching solution consists of a carefully balanced mixture of potassium hydroxide (KOH) dissolved in water with isopropyl alcohol (IPA). The ratio of isopropyl alcohol and potassium hydroxide controls the etch rate for the different silicon crystal planes. A solution of KOH dissolved in H_2O without IPA produces an etch rate which is fastest for the (110) planes then next fastest by the (100) and (111) planes, respectively, such that $R_{110} > R_{100} > R_{111}$. Here R_{xyz} represents the etch rate of a particular silicon crystal plane. Adding IPA however to the aqueous KOH solution can decrease the etch rates for (110) and (100) silicon planes by as much as 90% and 20% respectively, thereby reversing the etch rates as $R_{100} > R_{110} > R_{111}$. [11] The composition of the anisotropic etching solution can be adjusted to achieve nearly equal etching rates for (110) and (100) planes as $R_{110} \approx R_{100} > R_{111}$. The etch rate ratios between the (100) and (111) planes and the (110) and (111) planes are also of interest and these ratios can be as high 100:1 for a solution composed of 23 % KOH and 13 % IPA by weight. [12] An anisotropic liquid etching solution with $R_{110} \approx R_{100} > R_{111}$ would be nearly ideal for etching through the aperture in the mask in Fig. 9 to produce the silicon array of square based pyramidal mesa frustum pixels.

Anisotropic liquid etching with KOH:IPA:H_2O solution allows the precise and rapid fabrication of large area APD arrays with small pixel sizes for high spatial resolution imaging FPAs. The APD array design presented here has square pixels as shown in Fig. 9 with a side length of 27 µm and a mesa height of 10 µm. Although, smaller pixel sizes can be fabricated by anisotropic liquid etching, the fixed angle ϕ_c = 54.7° between the (100) and (111) planes in silicon constrains the mesa top area and the height of the mesa. Increasing the mesa height to improve the absorption efficiency of light in silicon reduces the mesa top area which needs to remain large enough to accommodate an indium metal solder bump of at least 15 μm in diameter in order not to sacrifice bump fabrication yields. A pixel size of 27 μm with mesa height h = 10 μm therefore represents a good compromise between the need for high resolution and light absorption efficiency while supporting a square mesa pixel top area with a side length of nearly 13 μm for reliable indium bump fabrication. [3]

3.1 Quantum efficiency of a crystallographically etched silicon APD pixel

High photodetector quantum efficiency is critical for APD device performance and is described by Eq. (5).

$$\eta_{eff} = (1 - R)\left[\left(1 - e^{-\alpha(\lambda)h}\right)\right]\zeta \tag{5}$$

Three terms in Eq. (5) contribute to the overall APD photodetector quantum efficiency including the optical power transmittance into silicon given by the first term, light absorption efficiency in silicon given by the second term and the collection efficiency ζ, of photogenerated electron-hole pairs (EHPs) that contribute to the photocurrent in the device. The optical power transmittance term $T(\lambda) = (1-R(\lambda))$ was calculated in Sec. 2.2 as a function of wavelength for TE polarized waves normally incident on the back-illuminated APD substrate. The absorption efficiency term $(1-e^{-\alpha(\lambda)h})$ in Eq. (5), describes the efficiency of light absorption in the device silicon and depends on the silicon mesa height h, and the silicon absorption efficiency $\alpha(\lambda)$. Electrical isolation of APD pixels by crystallographic etching results in a mesa geometry with non-uniform height that depends on position as h(x,y) where x and y are coordinates located in the square base plane area of the pixel. The effective absorption efficiency can be calculated for the APD pixel with non-uniform height for back-illuminated normally incident light, by integrating the absorption efficiency term from Eq. (5) over the pixel base area to yield the integration result I_{Ax} where x indexes a region of the base area, followed by a normalization of the result by the base area of the pixel as expressed in Eq. (6).

$$\eta_{abs} = \frac{8\left(I_{A1} + I_{A2}\right)}{\left(A_1 + A_2\right)} \tag{6}$$

The absorption efficiency η_{abs} is calculated most readily by integrating over one octant of the mesa pixel base area OMN shown in Fig. 10 and multiplying the final result after normalization by a factor of 8.

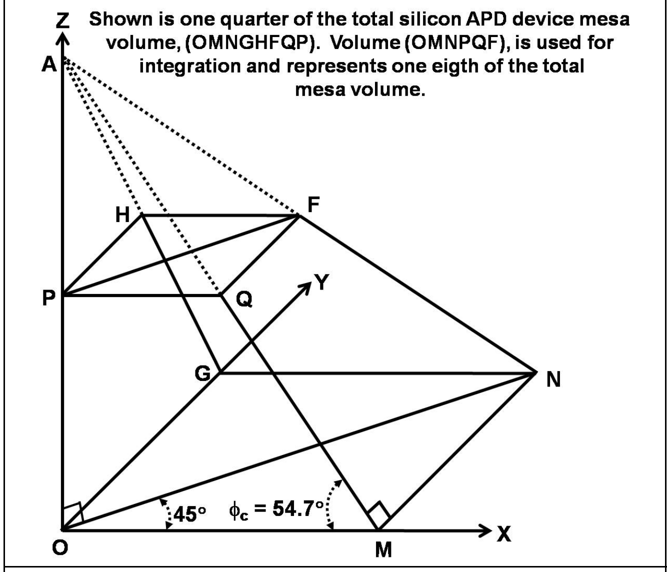

Fig. 10: *Mesa geometry used for integration to calculate I_{A1} and I_{A2} in equation* 6.

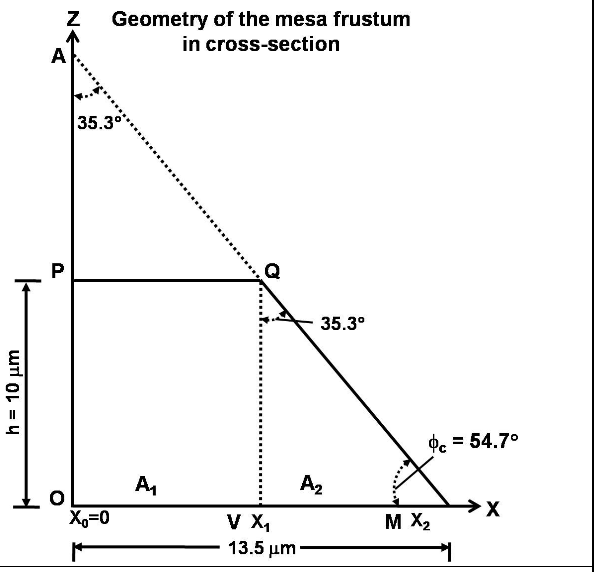

Fig. 11: *Two-dimensional cross section of the silicon mesa frustum in figure* 10.

Lidar Remote Sensing for Environmental Monitoring IX,
Edited by Upendra N. Singh, Kazuhiro Asai, Achuthan Jayaraman, Proc. of SPIE Vol. 7153, 71530Z

The calculated absorption efficiency of a back-illuminated, crystallographically etched silicon pixel mesa with 10 µm height is plotted in Fig. 12 for different pixel sizes showing the effects of silicon removal. Figure 13 shows the maximum attainable quantum efficiency of the APD pixel assuming uniform TE-wave back-illumination at normal incidence on the pixel base area through the substrate without a microlens and assuming ideal collection efficiency of photogenerated carriers in the device with $\zeta = 1$.

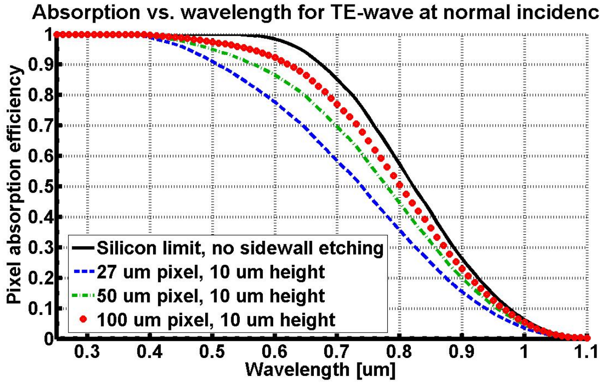

Fig. 12: Pixel absorption efficiency for different pixel sizes.

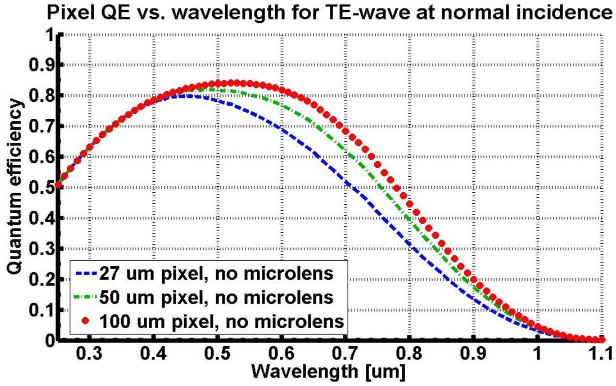

Fig. 13: Pixel quantum efficiency for different pixel sizes and height h=10µm.

The collection efficiency term zeta ζ in Eq. (5), represents the fraction of photogenerated EHPs contributing to photocurrent in the device, that are not lost to recombination at defect/trap sites or at the internal APD guard diode structure. A guard diode structure shown in Fig. 1 is necessary in a mesa isolated APD device to collect the surface generated electrons at the passivated (111) sidewalls, thereby preventing them from being transported to the device interior where they can be multiplied to increase device noise. Zeta becomes difficult to calculate precisely because information is needed about the trap species and their spatial concentrations in the device. Information about the spatial electric field in the device under bias conditions is also needed to describe photogenerated carrier drift either toward the high electric field multiplication region in the device or toward the guard diode at the periphery of the mesa that is intended ideally to collect only the surface generated noise electrons. For a two terminal APD with a guard diode, an expression for ζ is given by Eq. (7), where β represents the fraction of multiplied photoelectrons and γ represents the fraction of unmultiplied photoelectrons collected by the guard diode. The quantities β and γ sum to unity in the absence of recombination or other carrier loss mechanisms in the device.

$$\zeta = \beta + \frac{\gamma}{G} \tag{7}$$

The multiplication gain value G, appears in the denominator of Eq. (7) because photoelectrons collected by the guard diode are not multiplied by the avalanche gain of the APD and therefore the gain term in the denominator of Eq. (7) cancels the gain term that multiplies the overall APD quantum efficiency η_{eff} used in calculating the device photocurrent i_p. The photocurrent i_p includes a contribution from the multiplied and unmultiplied photoelectrons. [10] The quantum efficiency of the APD should always be calculated with G set to unity in Eq. (7).

A function $f_{gd}(x,y)$ shown in Fig. 1 that deterministically separates the internal regions of the APD where photogenerated electrons will be collected by the multiplication region or the guard diode is an idealization and does not exist in practice due to the probabilistic nature of charge carrier motion. In Sec. 4 of the paper however, the spatial electric field inside the APD is qualitatively studied at different reverse bias conditions, and the guard diode boundary can be at least in part identified based on the vector electric field lines in the device. A future goal of our research is to evaluate the ζ term in Eq. (5) by the Monte Carlo computational statistical method to obtain precise average values for β and γ for an APD, and to allow the excess noise factors of the internal APD gain G, and other random variables in the device such as β and γ to be accurately evaluated.

3.2 Improvement in APD array sensitive-area-fill-factor using monolithic sapphire microlenses

The etched mesa geometry characterized by crystallographic angle ϕ_c is necessary for electrically isolating the APD pixels in the array but also creates optical dead space by removing silicon between mesas which reduces the effective pixel height and therefore the absorption efficiency as shown in Fig. 12. The sapphire substrate however, allows the reduction in absorption efficiency of the APD pixels produced by mesa etching to be fully compensated by fabricating spherical microlenses directly in the thinned sapphire substrate as shown Fig. 1. The microlens focuses the optical field toward the interior full height region of the APD and away from the mesa sidewalls, thereby restoring the APD pixel absorption efficiency. Figure 14 shows light focusing by the microlens using three dimensional ray tracing of TE-polarized light at normal incidence to the back-illuminated pixel. The maximum theoretical quantum efficiency of the APD pixel is given by the black curve in Fig. 15 for a 27 μm pixel with h = 10 μm and no mesa etching. The dashed blue line is the same as in Fig. 13 for a mesa etched pixel without a microlens while the solid blue line shows the microlens restoring the quantum efficiency of the APD almost to the theoretical limit of the solid black line.

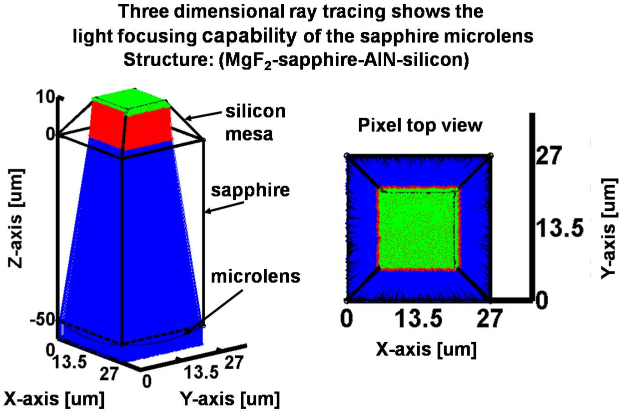

Fig. 14: Three-dimensional ray tracing in MATLAB for an APD pixel with microlens focusing light at normal incidence.

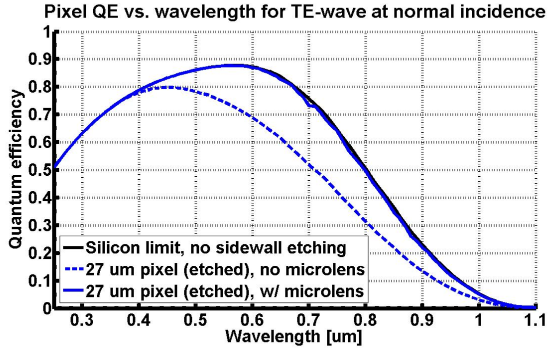

Fig. 15: Comparison of the APD pixel quantum efficiency without and with the monolithic sapphire microlens.

In addition to compensating the loss in APD pixel quantum efficiency resulting from the mesa isolation etch, the sapphire microlens also provides 100% sensitive-area-fill-factor for the APD array by focusing the extreme rays shown in red in Fig. 2 into the active volume of the pixel. Focusing of extreme rays to provide 100% sensitive-area-fill-factor for a 1024x1024 array of 27 μm APD pixels is only effective above a minimum threshold value of the camera lens focal ratio or f-number (f/#). The minimum focal ratio threshold is evaluated by translating the APD pixel in Fig. 14 the maximum distance from the optic axis to the corner of the array as shown in Fig. 16, and tracing rays located in-plane with the optic axis from the edge of the lens clear aperture to the pixel. Considering an infinite-finite conjugate imaging system with camera lens focal length fixed to F = 21 cm and a variable lens clear aperture, Fig. 17 plots the fractional area of the 1024x1024 pixel FPA with 100% sensitive-area-fill-factor as a function of the camera focal ratio setting.

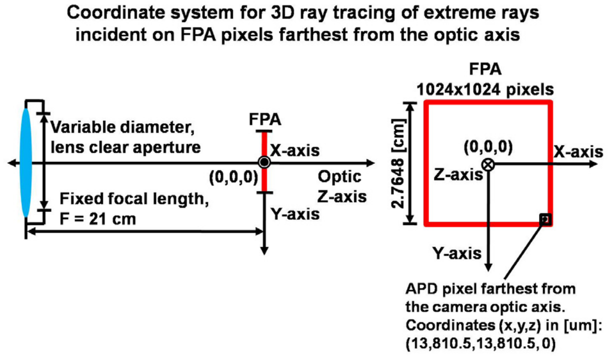

Fig. 16: Coordinate system for 3D ray tracing of extreme rays to evaluate the focusing capability of the microlenses.

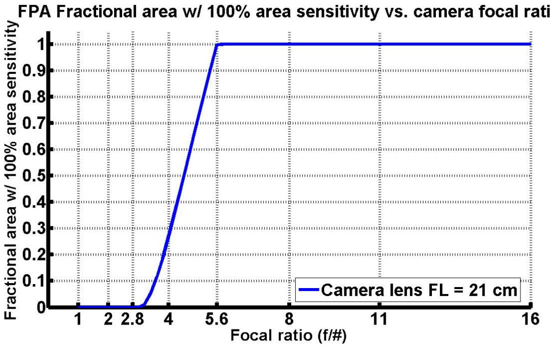

Fig. 17: A focal ratio of 5.6 provides 100% sensitive-area-fill-factor over the full 1024x1024 array of 27 μm pixels.

4. WIDE DYNAMIC RANGE SILICON MESA APD DESIGN

It can be shown that in order to image effectively under all ambient illumination ranging from the extreme AM0 condition in outer space when the APD-FPA imager is staring directly into the sun and the illuminance at the camera lens is approximately 130,000 Lux, to the photon starved case when imaging a scene on a cloudy night with no moon and far away from city lights when the illuminance at the camera lens might be 0.0001 Lux, the APD should be capable of operating in a dual mode, either in a linear mode with or without internal gain biased below the reverse breakdown voltage or in the single photon sensitive Geiger-mode biased above the reverse breakdown voltage. The APD mode of operation (analog linear or digital Geiger-mode) is selected by the requirement of maximizing the signal to noise ratio (SNR) of the APD-FPA optical receiver. [10,13] The linear mode of operation is appropriate when detected signals are large compared to the noise of the APD optical receiver and would cause the Geiger-mode APD to saturate such as in daylight imaging applications. By contrast, the Geiger-mode of operation provides large internal APD gain for single photon sensitivity and zero electronic readout noise which is needed for very low light level passive or active imaging. Geiger-mode operation is especially useful for active imaging when the photon returns from an object are well localized temporally as with a pulsed laser, and must be discriminated from background noise uniformly spread out in time.

Designing an APD that can operate with high quantum efficiency in both the analog linear mode with or without internal gain and in the digital Geiger-mode when biased above reverse breakdown voltage is difficult and has not been successfully implemented yet in a solid-state APD-FPA camera. To operate efficiently, such a device must deplete the p-type silicon fully to the sapphire interface at relatively low reverse bias in the linear mode without gain, to efficiently collect photogenerated electrons from absorbed ultra violet light within a few tens of nanometers from the silicon surface. As the reverse bias voltage is increased, the critical electric field (E_c = 3E5 V/cm) in silicon is reached in the more heavily doped multiplication region of the device. Impact ionization occurs above the critical electric field and produces avalanche gain which is useful for linear mode device operation with gain. As the reverse bias voltage is increased to the reverse breakdown voltage, the electric fields become sufficiently large to produce nearly infinite gain in the APD causing a large current to flow that can damage the pn-junction. Biasing the APD above the reverse breakdown voltage is possible however, using digital pixel control circuitry with active quenching that supports operation in the Geiger-mode with zero electronic readout noise. [2,3]

The mesa etched silicon APD design we developed is easy to fabricate and supports high quantum efficiency operation with wide dynamic range in the ultraviolet and visible wavelengths. The silicon APD fabrication simulations and device simulations were implemented using powerful commercial software on a UNIX workstation. The device simulation was based on the structure created by the fabrication simulation. Figure 18 shows the simulated APD device structure.

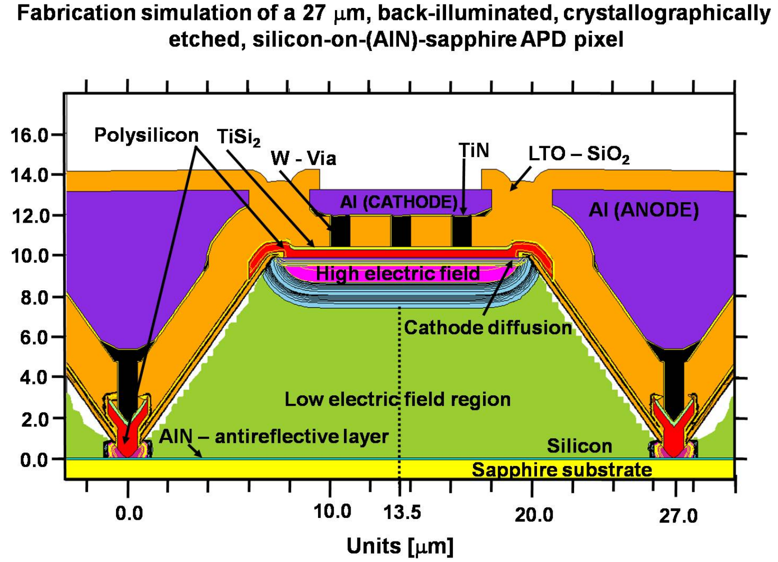

Fig. 18: Simulated silicon APD mesa device structure for arrays. The device is fabricated using crystallographically selective etching, thermal oxidation/diffusion, deposition, isotropic liquid etching and photolithography steps.

Lidar Remote Sensing for Environmental Monitoring IX,
Edited by Upendra N. Singh, Kazuhiro Asai, Achuthan Jayaraman, Proc. of SPIE Vol. 7153, 71530Z
CCC code: 0277-786X/08/$18 http://dx.doi.org/10.1117/12.804846

Wide dynamic range APD device operation is achieved by allowing the polysilicon cathode to extend beyond the edges of the mesa top over the thermally grown passivation oxide to form an MOS capacitor which acts as a CCD gate. When the APD is reverse biased, the combination of the APD pn-junction and the MOS capacitor formed by the overhanging polysilicon operate similarly to the input diode and input gate of a CCD. [1] At reverse bias voltages well below the reverse breakdown voltage of the APD, the APD pn-junction cannot deplete fully to the silicon-sapphire interface due to blocking by the high electric field boron impurity diffusion however, the polysilicon MOS capacitor can deplete into the p-type silicon fully to collect any photogenerated electrons in the device. The APD pn-junction prevents an inversion layer from forming under the polysilicon CCD gate by collecting the photoelectrons under the gate, producing an unmultiplied photocurrent. Therefore, at low reverse bias voltages the polysilicon MOS capacitor depletes deep into the silicon to collect photogenerated electrons which are in turn collected by the cathode of the APD pn-junction, bypassing the high electric field region of the APD without being multiplied. Figure 19 on the left shows the equipotential contours and electric field lines from device simulation at the low reverse bias voltage of 28 V, which is 8 Volts below the 36 V breakdown voltage of the APD. At low reverse bias, the photogenerated electrons are mainly directed toward the MOS capacitor at the periphery of the device and relatively few photogenerated electrons in the APD reach the high electric field multiplication region. Therefore, the internal gain of the device is low even though the electric field in the multiplication region does reach the critical value of 3E5 V/cm in silicon required for impact ionization.

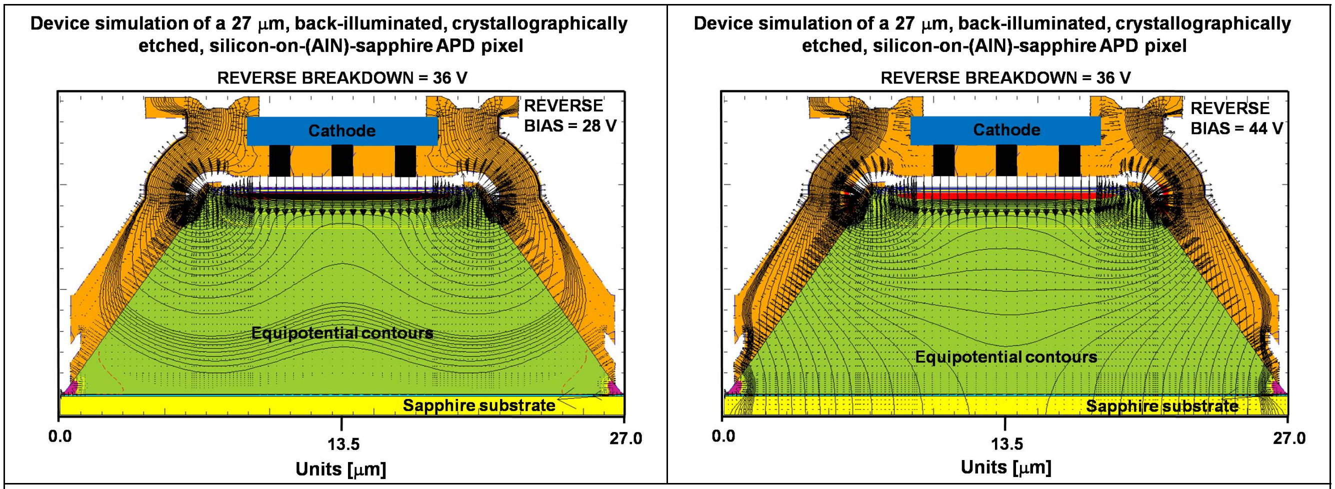

Fig. 19: APD device simulation showing equipotential contours and electric field lines for reverse bias voltages of 28 V (left) and 44 V (right). The reverse breakdown voltage of the APD is 36 V and the p-type silicon background resistivity is 100 Ω-cm.

Figure 19 on the right shows the equipotential contour change when the APD is reverse biased at 44 V, corresponding to an 8 V bias value above the reverse breakdown voltage of the APD. The result is a much larger fraction of photogenerated electrons directed toward the high electric field multiplication region of the APD than for the lower bias voltage on the left resulting in more internal gain. In both examples, the silicon is fully depleted to enable efficient collection of photogenerated electrons from the entire device volume.

CONCLUDING REMARKS

We have shown that a novel back-illuminated silicon APD array architecture using (100) epitaxial silicon grown on R-plane sapphire having a lattice matched AlN antireflective layer, provides a unique fabrication means for creating high quantum efficiency, wide dynamic range APD device arrays with monolithic sapphire microlenses for large area, high resolution, solid-state APD-FPA imagers with zero optical cross talk and 100% sensitive-area-fill-factor. Such APD-FPA imagers could be used for both passive and active 2D and 3D imaging applications. Our current research efforts are focused on optimizing the APD device design by Monte Carlo simulation with the goal of fabricating high performance device arrays.

REFERENCES

[1] Sze, S.M., [Physics of Semiconductor Devices 2nd Edition], John Wiley & Sons, New York, 495, 412-427, (1981).

[2] Stern, A., et al., “Scalable CMOS readout circuit architecture for photo-counting applications using Geiger-mode avalanche photodiodes,” Solid State Research Report MIT Lincoln Laboratory, (4), 25-30, (2001).

[3] Stern, A., et al., “Intensity-imaging focal plane array using Geiger-mode avalanche photodiodes,” Solid State Research Report MIT Lincoln Laboratory, (4), 23-31, (2003).

[4] McIntyre, R.J., “Multiplication Noise in Uniform Avalanche Diodes,” IEEE Trans. Electron Devices, ED-13(164), (1966).

[5] Lau, S.S., Matteson, S., Mayer, J.W., Revesz, P., Gyulai, J., “Improvement of Crystalline Quality of Epitaxial Silicon Layers by Ion-Implantation Techniques,” Applied Physics Letters, 34(1), (1979).

[6] Kronberg, M.L., “Plastic Deformation of Single Crystals of Sapphire: Basal Slip and Twinning,” Acta Metall., 5(507), (1957).

[7] Shibata, T., Asai, K., Nakamura, Y., Tanaka, M., Kaigawa, K., Shibata, J., Sakai, H., “AlN epitaxial growth on off-angle R-plane sapphire substrates by MOCVD,” J. of Crystal Growth, 229(1), 63-68, (2001).

[8] Luo, W., Wang, X., Guo, L., Xiao, H., Wang, C., Ran, J., Li, J., Li, J., “Influence of AlN buffer layer thickness on the properties of GaN epilayer on Si(111) by MOCVD,” Microelectronics Journal, Jan., (2008).

[9] Ozgür, Ü., Webb-Wood, G., Everitt, H.O., Yun, F., Morkoc, H., “Systematic measurement of $Al_xGa_{1-x}N$ refractive indices,” Applied Physics Letters, 79(25), (2001).

[10] Saleh, B.E.A., Teich, M.C., [Fundamentals of Photonics], John Wiley & Sons, New York, 246-253, 755, 789, (2007).

[11] Seidel, H., Cspergi, L., Heuberger, A., Baumgärtel, H., “Anisotropic Etching of Crystalline Silicon in Alkaline Solutions,” J. Electrochem. Soc., 137(11), 3612-3625 (1990).

[12] Plummer, J.D., Deal, M.D., Griffin, P.D., [Silicon VLSI Technology], Prentice Hall, Upper Saddle River NJ, 618-619, (2000).

[13] Stern, A.G., (Ph.D. thesis calculations)

Lidar Remote Sensing for Environmental Monitoring IX,
Edited by Upendra N. Singh, Kazuhiro Asai, Achuthan Jayaraman, Proc. of SPIE Vol. 7153, 71530Z

CCC code: 0277-786X/08/$18 http://dx.doi.org/10.1117/12.804846